Volume 1 | Number 1 | Jan 2013 | Pages 1–100

Nanoscale

www.rsc.org/nanoscale

ROYAL SOCIETY
OF CHEMISTRY

ROYAL SOCIETY
OF CHEMISTRY

www.rsc.org/nanoscale

Nanoscale

ARTICLE

Hierarchical SrTiO₃/NiFe₂O₄ composite nanostructures with excellent light response and magnetic performance synthesized toward enhanced photocatalytic activity

Panpan Jing,[a] JinLu Du,[a] Jianbo Wang,[a,b] Wei Lan,[a] Lining Pan,[a] Jianan Li,[a] Jinwu Wei,[a] Derang Cao,[a] Xinlei Zhang,[a] Chenbo Zhao[a] and Qingfang Liu[a*]

Being capable of gathering advanced optical, electrical and magnetic properties originated from different components, multifunctional composite nanomaterials have been concerned increasingly. Herein, we have successfully demonstrated the preparation of SrTiO₃/NiFe₂O₄ porous nanotubes (PNTs) and SrTiO₃/NiFe₂O₄ particles-in-tubes (PITs) via a single-spinneret electrospinning and a side-by-side-spinneret electrospinning, respectively. The products were characterized by using scanning electron microscopy, transmission electron microscopy, X-ray diffraction, UV-visible diffuse reflectance spectra and vibrating sample magnetometer in detail. The results indicate that SrTiO₃/NiFe₂O₄ PNTs are the heterojunction nanotubes by connecting perovskite SrTiO₃ and spinel NiFe₂O₄ nanoparticles, but SrTiO₃/NiFe₂O₄ PITs are the self-assembled core/shell structures by embedding SrTiO₃ nanoparticles into NiFe₂O₄ nanotube. Compared with pure SrTiO₃ nanofibers, the two SrTiO₃/NiFe₂O₄ composites exhibit a powerful light response and an excellent room temperature ferromagnetism. The magnetic separations directly reveal that such amazing recycling efficiencies of about 95% for SrTiO₃/NiFe₂O₄ PNTs and about 99.5% for SrTiO₃/NiFe₂O₄ PITs are obtained. Furthermore, both of the two magnetic composites perform the considerable photocatalytic activity in the degradation of rhodamine B. We propose that Kirkendall-diffusion and phase-separation are probably responsible for the formation of SrTiO₃/NiFe₂O₄ PITs, and this work could provide a feasible way to assemble the core/shell structures of different materials.

Introduction

One-dimensional (1D) composite nanomaterials have attracted a growing research interest due to their multifunctional advantages for modern technological applications including photocatalysis,[1] lithium-ions batteries,[2] biomedicine,[3] electromagnetic and optical devices.[4-6] To date, various 1D nanocomposites have been prepared by hydrothermal method, chemistry vapor deposition and so forth.[7-9] However, these methods are either of expensive, tedious or condition rigorous in procedure. In contrast, electrospinning has been certified as a more accessible, efficient and flexible approach, which is widely used in the energy-relation applications, sensor, drug delivery and tissue engineering technique.[10-13] At a lab, a typical electrospinning equipment can be simply assembled by a high-voltage power supply, a syringe, a flat tip needle and a conductive collecting screen.[12] Ever since it became extraordinarily popular, electrospinning has been utilized to fabricate all kinds of 1D continuous organic/organic, organic/inorganic and inorganic/inorganic composites. For instance, A.V. Bazilevsky and K.M. Forward severally reported the PMMA/PAN and (PEO+PEG)/PS core-shell nanofibers by single-nozzle co-electrospinning and needleless electrospinning.[14, 15] T. Fiorido and T.T. Jiang investigated the sensing performance of PU/Fe₃C@C and SnO₂/PPy hybrid nanofibers obtained through

electrospinning route, respectively.[16, 17] Z.Y. Liu and F. Xu successfully prepared the side-by-side TiO₂/SnO₂ heterojunctions via a dual-spinneret and a dual-opposite-spinneret electrospinning.[18, 19] All of these nanocomposites have well-controlled morphologies, uniform chemical components and diameter distributions.

Over the past few years, with the aggravation of environment pollution and the excessive consumption of non-renewable energy sources (coal and fossil oil), significant achievements have been acquired from the researches of contaminants removal and hydrogen (H₂) generation by using the eco-friendly photocatalytic technique, which is based on the "advanced oxidation process (AOP)".[20, 21] Out of the numerous semiconductor photocatalysts, strontium titanate (SrTiO₃) is a promising candidate for the photocatalytic technique because of its high catalytic activity, strong photo-corrosion resistibility and good structural stability.[22, 23] In industry practical operations, generally, a huge amount of the used catalyst powders should be recycled from the as-purified water timely and completely, otherwise their residuum maybe result in a secondary pollution.[24] Moreover, recycling is another consideration for evaluating an ideal photocatalyst. To solve this problem, filtration and adsorption have been widely used.[25, 26] But they do not work well for separating the powdered photocatalysts with a good dispersion in aqueous systems. Recent investigations have pointed out that some advanced magnetic

photocatalysts, such as Fe_3O_4-$FeWO_4$ p-n junction,[27] gamma-Fe_2O_3/TiO_2 hollow bowls,[28] $CoFe_2O_4$/Bi_2WO_6 composites[29] and $Bi_{25}FeO_{40}$-graphene composites,[30] could effectively overcome the hard separation by an applied magnetic field. Thus, developing novel $SrTiO_3$-based composite photocatalysts by compounding $SrTiO_3$ and other magnetic materials will be a much encouraging topic. As one of the well-known magnetic materials, spinel nickel ferrite ($NiFe_2O_4$) has been extensively studied not only owing to its useful magnetic and electrical properties such as moderated saturation magnetization and electrical resistivity, but also owing to its desirable chemical and structure stability and a good sunlight absorption.[31-33] It predicts that $NiFe_2O_4$ has an attractive prospect in the photocatalytic field.[33, 34] Thus, magnetic $SrTiO_3$/$NiFe_2O_4$ composite photocatalysts could be an inspiring suggestion. Nevertheless, 1D $SrTiO_3$/$NiFe_2O_4$ composite nanostructures have not been investigated systemically by far, as well as the scarcity in the other reported literatures.

For the first time in this current work, the novel $SrTiO_3$/$NiFe_2O_4$ porous nanotubes (PNTs) and $SrTiO_3$/$NiFe_2O_4$ nanoparticle-in-nanotubes (PITs) were respectively prepared via a single-spinneret electrospinning and a side-by-side-spinneret electrospinning, and their chemical components, microstructures, optical and magnetic properties, magnetic recyclability and photocatalytic activities were investigated in detail.

Experimental

Materials

Main chemical reagents of polyvinylpyrrolidone (PVP), tetrabutyl titanate ($Ti(C_4H_9O)_4$), strontium nitrate ($Sr(NO_3)_2$), nickel nitrate hexahydrate ($Ni(NO_3)_2 \cdot 6H_2O$), iron nitrate nonahydrate ($Fe(NO_3)_3 \cdot 9H_2O$) and *N,N*-dunetgyl formamide (DMF) were analytical grade and used without any further purification.

Synthesis of $SrTiO_3$/$NiFe_2O_4$ PNTs and $SrTiO_3$/$NiFe_2O_4$ PITs

The two composites of $SrTiO_3$/$NiFe_2O_4$ PNTs and $SrTiO_3$/$NiFe_2O_4$ PITs were severally synthesized by a traditional single-spinneret electrospinning[12] and a modified side-by-side-spinneret electrospinning, of which the schematic diagram is shown in Fig. 1. A typical preparation is depicted as below. The first step is preparing the spinning solutions. Stoichiometric $Ti(C_4H_9O)_4$ and $Sr(NO_3)_2$ with mole ratio of 1:1 and 0.3 g PVP were dissolved in a mixed solvents of 1.25 g C_2H_5OH, 0.6 g deionized water, 1.5 g DMF and 1.5 g CH_3COOH under vigorous stirring for overnight to obtain solution A. Similarly, stoichiometric $Ni(NO_3)_2 \cdot 6H_2O$ and $Fe(NO_3)_3 \cdot 9H_2O$ with mole ratio of 1:2 and 0.3g PVP were dissolved in another co-solvents of 2.43 g C_2H_5OH and 1.62 g deionized water to obtain solution B. The second step is electrospinning. To prepare the precursor nanofibers Ⅰ of $SrTiO_3$/$NiFe_2O_4$ PNTs, the equal amounts of solutions A and B were homogenously mixed together and then was loaded into a glass syringe with the single-spinneret. The solution was propelled by applying a micro-injection pump with a constant rate of 0.3 mL/h. The vertical distance and voltage difference between the nozzle tip and the grounded stainless collector were fixed at about 19 cm and 16 kV, respectively. Several hours later, a uniform nanofiber met was deposited on the collector. On the other hand, another equal volumes of solutions A and B were transferred alone into the each syringe of the side-by-side-spinneret electrospinning apparatus (Fig. 1). Under the same condition of the above single-spinneret electrospinning process, the precursor nanofibers Ⅱ of $SrTiO_3$/$NiFe_2O_4$ PITs were spun. All electrospinning experiments were conducted at room temperature in air. During the heating treatment of the third step, both of the as-

spun precursor nanofibers Ⅰ and Ⅱ were subjected at 80 ℃ for a few hours followed by annealing at 600 ℃ for another 2 h in a muffle furnace. When the furnace cooled down to room temperature, the $SrTiO_3$/$NiFe_2O_4$ PNTs and $SrTiO_3$/$NiFe_2O_4$ PITs were obtained. The heating rate and cooling rate were set at 1 ℃/min. Furthermore, the pure $SrTiO_3$ nanofibers (NFs) and pure $NiFe_2O_4$ nanotubes (NTs) were also acquired according to the single-spinneret electrospinning process.
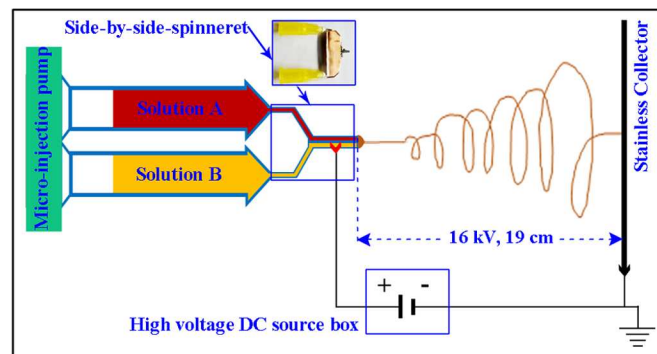

Fig. 1 Diagrammatic top view of the side-by-side-spinneret (the inset) electrospinning apparatus.

Characterization

The phase components and crystalline structures of $SrTiO_3$/$NiFe_2O_4$ PNTs and $SrTiO_3$/$NiFe_2O_4$ PITs were detected by X-ray diffraction (XRD, Cu Ka1, λ=1.5406 Å, PANalytical X' Pert Pro), high-resolution transmission electron microscopy (HRTEM, Tecnai™ G^2 F30, FEI) and selected area electron diffraction (SAED) system. Feld emission scanning electron microscopy (FESEM, Hitachi S-4800), transmission electron microscopy (TEM), high-angle annular dark-field and scanning transmission electron microscopy (HADDF-STEM) were applied to observe the surface morphologies and internal microstructures. Their room temperature magnetic hysteresis (RT *M-H*) loops and UV-visible diffuse reflectance spectra (DRS) were measured on a vibrating sample magnetometer (VSM, Lakeshore 7403) and a TU-1901 spectrophotometer, respectively.

Magnetic separation and photocatalytic activity evaluations of $SrTiO_3$/$NiFe_2O_4$ PNTs and $SrTiO_3$/$NiFe_2O_4$ PITs

To evaluate the magnetic separation efficiencies accurately, each 100 mg $SrTiO_3$/$NiFe_2O_4$ PNTs and $SrTiO_3$/$NiFe_2O_4$ PITs powders were respectively added into a 20 mL deionized water. These two mixed solutions were stirred for about 30 min to achieve a fully-dispersive state before separation, for which a calibrated electronic timer and a square magnet with a field about 300 mT were used. The separation efficiencies were calculated by the formula of $(m_t/m_0) \times 100\%$ (m_t is the recycled mass of the sample at time t, m_0 = 100 mg is the initial mass).

The photocatalytic properties of $SrTiO_3$/$NiFe_2O_4$ PNTs and $SrTiO_3$/$NiFe_2O_4$ PITs were evaluated by a liquid-phase decomposition of the rhodamine B (RhB) solution under UV-visible light irradiation of a high-pressure xenon lamp. The initial volume of RhB solution was 50 mL with an initial concentration of 10 mg/L and a photocatalyst loading of 25 mg. Before irradiation, the mixed solution was stirred acutely in the dark for 1 h to reach a good adsorption-desorption equilibrium between photocatalyst and RhB molecules. At given irradiation intervals of 20 min during the photocatalytic process, an approximately 5 mL suspension was sampled and the contained $SrTiO_3$/$NiFe_2O_4$ powders were recycled by the above mentioned magnet. After photocatalytic degradation,

the concentration changes of RhB solutions were monitored by the spectrophotometer. Further, the cycling tests were also carried out to survey the catalytic endurance of these two magnetic photocatalysts.

Results and discussion

XRD patterns were used to determine the phase composition and crystalline size of samples. In Fig. 2(a) and 2(b), all the labelled diffraction peaks of corresponding samples could be indexed to the perovskite $SrTiO_3$ with cubic symmetry of Pm-3m (221) space group (JCPDS no. 35-0734) and the standard inverse spinel $NiFe_2O_4$ with cubic symmetry of Fd-3m (227) space group (JCPDS no. 54-0964), respectively. Therefore, both of the pure $SrTiO_3$ and pure $NiFe_2O_4$ are prepared without any other additives by the single-spinneret electrospinning. But, they are polycrystalline. After evenly blending their precursor-sols of the above two pure samples followed by the same preparation process, the signals of perovskite $SrTiO_3$ and inverse spinel $NiFe_2O_4$ are tracked together in the XRD pattern of the obtained sample shown in Fig. 2(c). In Fig. 2(d), moreover, the $SrTiO_3$ and $NiFe_2O_4$ phases are also simultaneously contained in the sample prepared by the side-by-side-spinneret electrospinning. Thus the $SrTiO_3/NiFe_2O_4$ composites are successfully fabricated through the two kinds of electrospinning routes. Compared with the pure $SrTiO_3$ and pure $NiFe_2O_4$, the diffraction peaks of both $SrTiO_3$ and $NiFe_2O_4$ phases in the XRD patterns of the two $SrTiO_3/NiFe_2O_4$ composites are weaker and broader. According to Debye-Scherrer equation,[35] the average crystalline sizes of $SrTiO_3$ and $NiFe_2O_4$ are respectively calculated to be about 16 nm and 11.5 nm for the $SrTiO_3/NiFe_2O_4$ composites shown in Fig. 2(c). For another composites shown in Fig. 2(d), that of $SrTiO_3$ and $NiFe_2O_4$ are calculated to be about 20 nm and 14 nm, respectively.
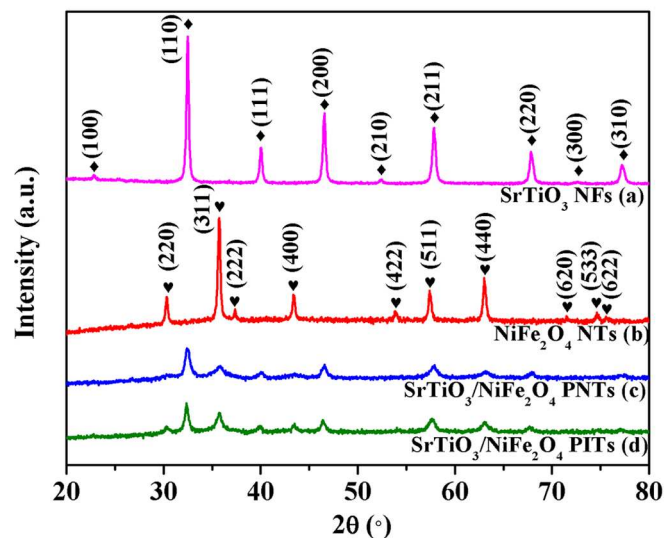

Fig. 2 Typical XRD patterns of (a) pure $SrTiO_3$ NFs, (b) pure $NiFe_2O_4$ NTs and (c) $SrTiO_3/NiFe_2O_4$ PNTs by using single-spinneret electrospinning and (d) $SrTiO_3/NiFe_2O_4$ PITs by using side-by-side-spinneret electrospinning.

The overall morphologies of the pure $SrTiO_3$, pure $NiFe_2O_4$ and two $SrTiO_3/NiFe_2O_4$ composites were observed by FESEM images exhibited in Fig. 3(a-d) firstly. It is evident that large quantities of typical filiform nanostructures are observed for all of these samples. They are tens of microns in length and random orientation. But each of them has unique characteristics. As shown in Fig. 3(a) and 3(b), the pure $SrTiO_3$ NFs with really smooth surface are tortuous along the long-axis direction but the pure $NiFe_2O_4$ NTs (seeing the inset) with slightly rough surface are straight. By counting more than 50 individuals, their average diameters are estimated to be about 81 nm

and 96 nm, respectively. For the $SrTiO_3/NiFe_2O_4$ composites (Fig. 3(c)) prepared by the single-spinneret electrospinning, abundant of uniform pores regularly distribute on their surface (seeing the inset). It is generally known that such an excellent porous nature not only tremendously promotes the contaminant molecules transfer but also provides more accessible sites for the photocatalytic reactions.[24] In regard to the $SrTiO_3/NiFe_2O_4$ composites (Fig. 3(d)) obtained by the side-by-side spinneret electrospinning, it can be found that this sample presents satisfactory hollow structure rather than the side-by-side dual fibre groups as previously reports.[18, 19] The average fibre diameter is similar to that of the pure $NiFe_2O_4$ NTs. In addition, both of the two $SrTiO_3/NiFe_2O_4$ composites are well dispersive.

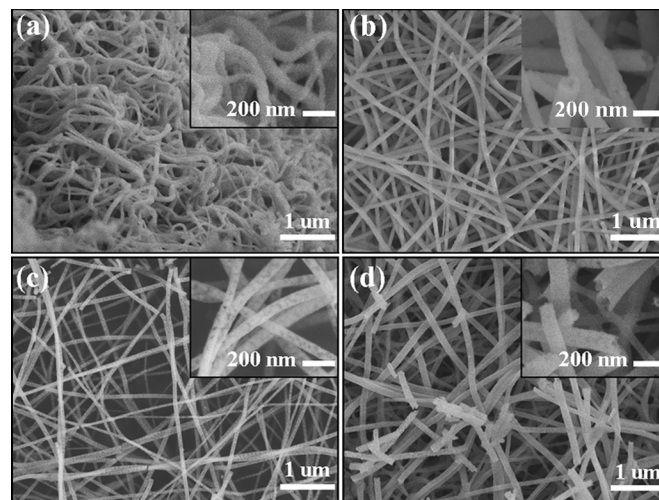**Fig. 3** Typical FESEM images of (a) pure $SrTiO_3$ NFs, (b) pure $NiFe_2O_4$ NTs and (c) $SrTiO_3/NiFe_2O_4$ PNTs using single-spinneret electrospinning and (d) $SrTiO_3/NiFe_2O_4$ PITs using side-by-side-spinneret electrospinning.

To get more detailed insights into the microarchitectures of the two $SrTiO_3/NiFe_2O_4$ composites, TEM analysis was carried out further. As examined in Fig. 4(a), the typical TEM images not only certify the distinctive porous feature but reveal the hollow structure of the $SrTiO_3/NiFe_2O_4$ composite nanofibers fabricated by using the single-spinneret electrospinning. Actually, the tiny pores are mainly caused by the PVP decomposition during annealing. Herein, we name this sample as $SrTiO_3/NiFe_2O_4$ porous nanotubes (PNTs). Fig. 4(b) is a HRTEM image of the $SrTiO_3/NiFe_2O_4$ PNTs. It shows clearly that $SrTiO_3$ and $NiFe_2O_4$ nanoparticles are closely connected with each other. That is, the $SrTiO_3/NiFe_2O_4$ PNTs also can be considered as the famous heterojunctions. The SAED pattern (Fig. 4(b)) contains two sets of diffraction rings and further indicates the polycrystalline nature of the $SrTiO_3/NiFe_2O_4$ PNTs. The first set of diffraction rings (cyan circles) composed of bright spots are indexed to the (110), (200) and (211) of $SrTiO_3$. While another set (white circles) are indexed to the (311), (400) and (440) of $NiFe_2O_4$. For $SrTiO_3/NiFe_2O_4$ PIT fabricated by using the side-by-side-spinneret electrospinning, the TEM image (Fig. 4(c)) is another powerful evidence for their tubular structures observed from the SEM image (Fig. 3(d)). Besides, it is fascinating that lots of bigger nanoparticles are situated in the nanotube axis and are isolated from the tube inner wall. The average nanoparticles sizes in the interior and on the walls of these tubes are estimated to about 37 nm and 13 nm, respectively. The HRTEM images (Fig. 4(d-f)) show the lattice fringes of three randomly selected parts on a PIT (the inset in Fig. 4(c)) and declares that $SrTiO_3$ nanoparticles stack along the interior axis of $NiFe_2O_4$ nanotubes. Using the side-by-side-spinneret electrospinning, hence,

the hierarchical $SrTiO_3/NiFe_2O_4$ PITs are successfully prepared, and their particle-in-tube structures are further certified by the HADDF-STEM image shown in Fig. 4(g). For the composite photocatalysts with core-connected-shell structures, it is always learned that the cores are magnetic materials and the shells are catalytic materials. During the photocatalytic reaction experiment, the structure of catalytic materials would be damaged because they are robustly scoured by the corrosive substances solution for a long time. On the other hand, if the shells are magnetic materials in some cases, the reactions between catalytic materials and pollutants will be interfered to some extent. Consequently, the synthesized novel $SrTiO_3/NiFe_2O_4$ PITs ($SrTiO_3$ nanoparticles in $NiFe_2O_4$ nanotube) could not only protect the structure of $SrTiO_3$ by the $NiFe_2O_4$ shell but also guarantee the catalytic reaction because the containment molecules can smoothly reach to the $SrTiO_3$ nanoparticles surface through the $NiFe_2O_4$ nanotube channel.
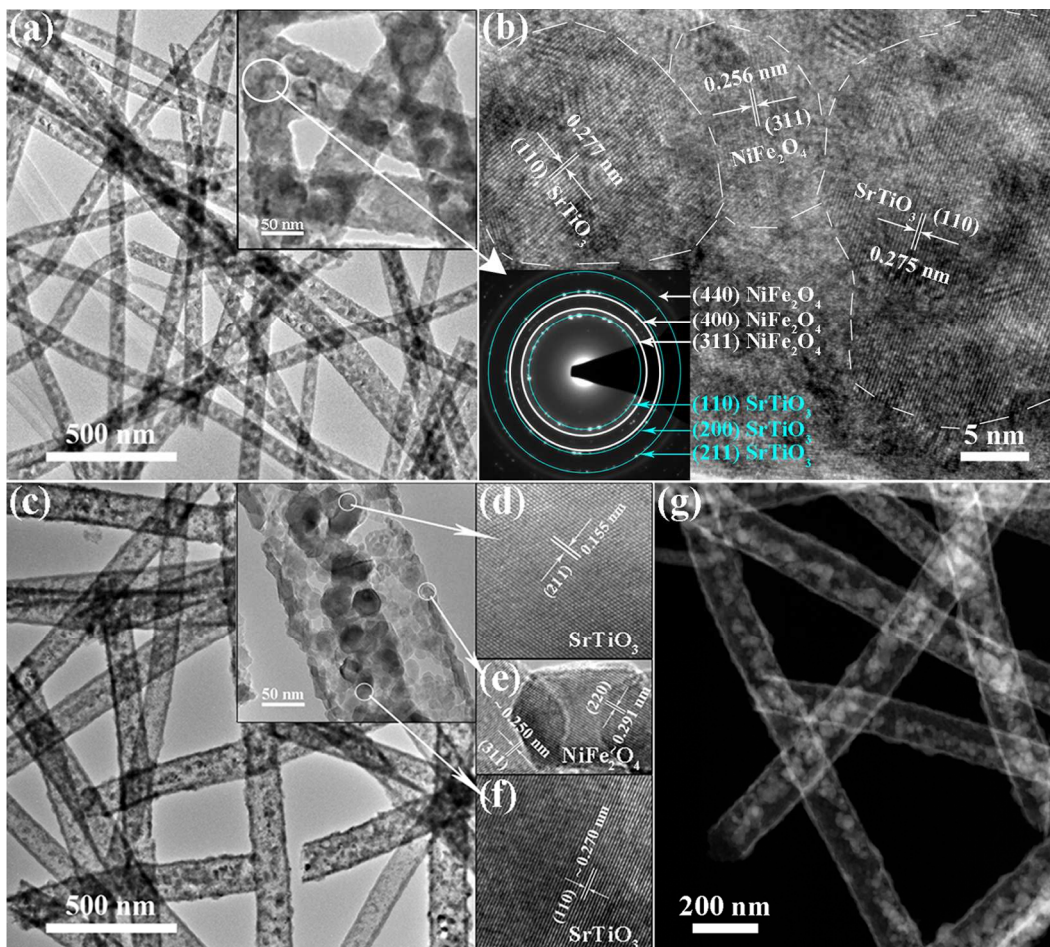

Fig. 4 (a) TEM and (b) HRTEM images for the $SrTiO_3/NiFe_2O_4$ PNTs, the inset in (b) is the SAED pattern; (c) TEM, (d-f) HRTEM and (g) HADDF-STEM images for the $SrTiO_3/NiFe_2O_4$ PITs. The insets in (a) and (c) are the corresponding magnification TEM images.

Fig. 5(a) shows the UV-vis DRS of the four samples to reveal their optical properties. The absorption band sharply drops at about 388 nm for the pure $SrTiO_3$ NFs, whereas that of the pure $NiFe_2O_4$ NTs continuously extends to the visible-light region (400 nm $< \lambda <$ 800 nm). This means that $SrTiO_3$ only has a response to the UV light but the pure $NiFe_2O_4$ NTs can response to both of the UV light and visible light. Using Tauc's equation $((\alpha h v)^2 = A(h v - E_g))$,[33] the band gaps ($E_g$) of pure $SrTiO_3$ NFs and pure $NiFe_2O_4$ NTs are calculated to be 3.2 eV and 1.7 eV, respectively, which basically conforms to the previous studies. [36, 33] The slight errors maybe result from the difference of the grain size.[37] Regarding the two composites of $SrTiO_3/NiFe_2O_4$ PNTs and $SrTiO_3/NiFe_2O_4$ PITs, they also have an enhanced absorption in UV and visible light region. Therefore, compounding $NiFe_2O_4$ with $SrTiO_3$ could effectively increase the utilization of irradiated lights with long wavelength. Interestingly, it is noteworthy that the characteristic absorption peak of $NiFe_2O_4$ at about 745 nm falls sharply in the DRS of $SrTiO_3/NiFe_2O_4$ PNTs but still excites in that of $SrTiO_3/NiFe_2O_4$ PITs. This two cases are

separately similar to the earlier reports about the $NiFe_2O_4@TiO_2$ and $TiO_2/SiO_2/NiFe_2O_4$ composite nanoparticles.[38,39] From this point of view, the heterojunctions of $SrTiO_3/NiFe_2O_4$ PNTs and particles-in-tube structures of $SrTiO_3/NiFe_2O_4$ PITs are certified further. Besides the optical property, possessing a good magnetic performance is also significant to the magnetic photocatalysts. As shown in Fig. 5(b), the recorded RT M-H loops reveal that the pure $SrTiO_3$ NFs have no any magnetism, but the $SrTiO_3/NiFe_2O_4$ PNTs and $SrTiO_3/NiFe_2O_4$ PITs both follow a ferromagnetic behaviour as well as the pure $NiFe_2O_4$ NTs with the saturation magnetization (M_s) of about 39 emu/g. Owing to presence of the non-magnetic $SrTiO_3$, the M_s values for the composite PNTs and PITs are lower than that of pure $NiFe_2O_4$ NTs and they are about 10 and 18 emu/g, respectively. Fig. 5(c) shows digital photographs taken at different times during the two $SrTiO_3/NiFe_2O_4$ composites magnetic separation from the deionized water. Of which, the recycling efficiencies of $SrTiO_3/NiFe_2O_4$ PNTs and $SrTiO_3/NiFe_2O_4$ PITs are about 95 % within 2.5 min and about 99.5% within 1 min, respectively. Thus both of the $SrTiO_3/NiFe_2O_4$

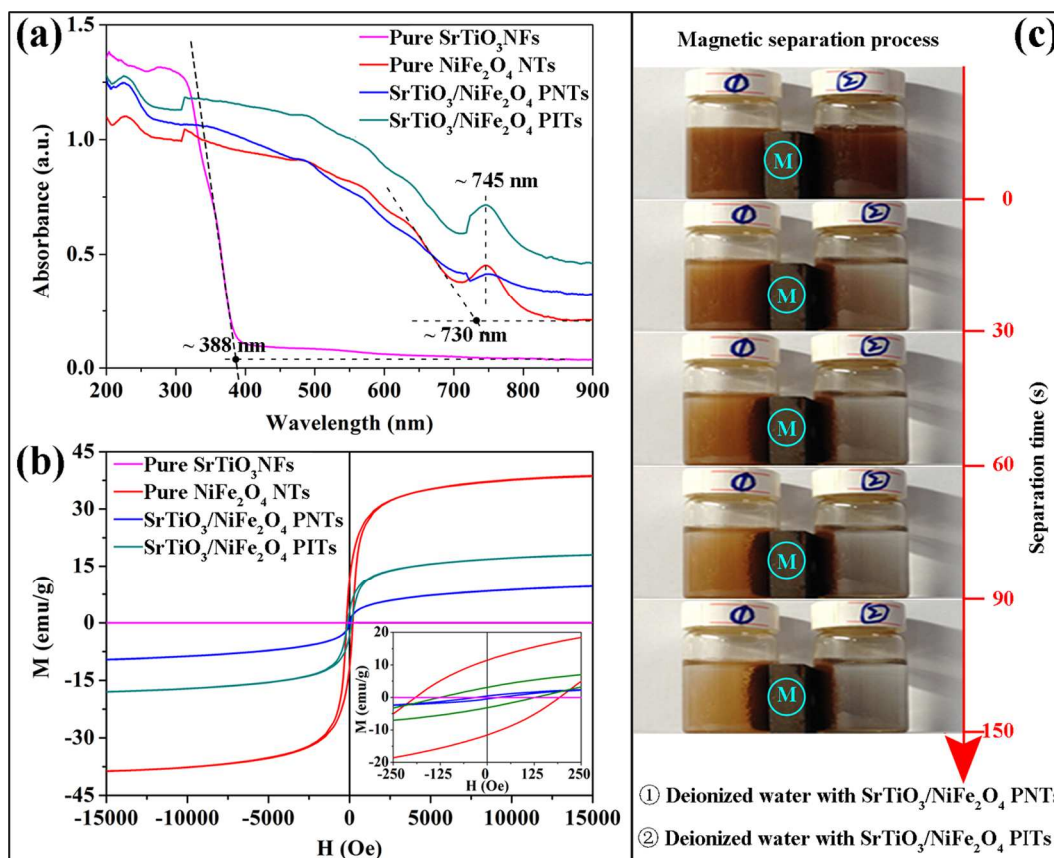PNTs and SrTiO$_3$/NiFe$_2$O$_4$ PITs have an amazing magnetic separation property.

Fig. 5 (a) UV-vis DRS and (b) RT *M-H* loops of the pure SrTiO$_3$ NFs (pink line), pure NiFe$_2$O$_4$ NTs (red line), SrTiO$_3$/NiFe$_2$O$_4$ PNTs (blue line) and SrTiO$_3$/NiFe$_2$O$_4$ PITs (green line). (c) The digital photographs taken at different times during the two SrTiO$_3$/NiFe$_2$O$_4$ composites magnetic separation from deionized water at different times.

As revealed above, it is expected that the SrTiO$_3$/NiFe$_2$O$_4$ PNTs and SrTiO$_3$/NiFe$_2$O$_4$ PITs could perform a satisfying photocatalytic activity in the liquid-phase decomposition of the RhB solution under the light irradiation. RhB is a typical artificial aromatic compound dye with a molecular formula C$_{28}$H$_{31}$ClN$_2$O$_3$ and is commonly used as a colour additive in industry. But it is highly venomous and probably causes cancer.[40] Large amount of RhB dyes released in the industrial wastewater, which is a toxic pollution source, is very dangerous. Hence the decomposition of RhB with cost-effective technique is very important and is always used to evaluate the catalytic performance of photocatalysts. Fig. 6(a) and (b) show the decomposition behaviours of RhB solution over the photocatalysis of SrTiO$_3$/NiFe$_2$O$_4$ PNTs and SrTiO$_3$/NiFe$_2$O$_4$ PITs, respectively. The peak intensity of the characteristic absorption at about 552. 4 nm is found to be decreased with the irradiation time and no new absorption band produces. Fig. 6(c) highlights the photo-decomposition efficiency (C_t/C_0, C_0 and C_t respectively present the initial concentration and instantaneous concentration of RhB dye) of RhB after 2 h of irradiation under different conditions. Little decomposition of RhB detected in the absence of any photocatalysts means that RhB dye is very stable and its self-decomposition can be neglected. When using the pure SrTiO$_3$ NFs, only about half of RhB is degraded. In contrast, the degradation of RhB is significantly increased to 99% and 83% over the SrTiO$_3$/NiFe$_2$O$_4$ PNTs and SrTiO$_3$/NiFe$_2$O$_4$ PITs, respectively. In both cases, in addition, it is noticed that there is a considerable amount of RhB vanished before irradiation, which should be attributed to the strong adsorption

abilities of the two composite photocatalysts, further indicating their high surface areas. Fig. 6(d) and (e) display the XRD patterns and SEM images of the magnetically recycled SrTiO$_3$/NiFe$_2$O$_4$ PNTs and SrTiO$_3$/NiFe$_2$O$_4$ PITs after the first photocatalytic reaction. It is hardly found remarkable changes of the phase and hollow structure compared with that of before reaction. Thus the two photocatalysts have a remarkable composition and microstructure stability and they are continuously execute twice photocatalytic experiments again. As depicted in Fig. 6(f) and (g), the recycling tests demonstrate that the two magnetic photocatalysts are both of amazing photocatalytic endurance because there is no obvious decrease in activity. As is known to all, the decomposition mechanism of the harmful dyes by photocatalysts mainly depends on the oxidation actions between the strongly oxidative ions and the dye molecules. [20] Of which, the oxidative ions are mainly the photo-excited holes (h$^+$), the hydroxyl radicals (·OH) and the super oxygen ions (O$_2^-$) respectively caused by the combination of photo-excited electrons (e$^-$) with hydroxyl ions (OH$^-$) and oxygen molecules (O$_2$) in the solution. According to the microstructure characterization and UV-vis spectra, the enhanced photocatalytic capacities of the SrTiO$_3$/NiFe$_2$O$_4$ PNTs and SrTiO$_3$/NiFe$_2$O$_4$ PITs compared with pure SrTiO$_3$ NFs in this work should be attributed to a few reasons as below. First, the porous and hollow structures of the two composite photocatalysts with lager surface areas can offer more reaction sites for the above mentioned oxidative ions and RhB molecules. Second, the strong response in the UV and visible light region greatly increased generation rate of the photo-excited h$^+$ and e$^-$. Third, the SrTiO$_3$/NiFe$_2$O$_4$ PNTs have a

higher survival rate of the photo-excited h^+ and e^-. Fig. 6(h) and (i) shows the schematic illustrations of the energy band structures and the photon-excited h^+ and e^- separations in the $SrTiO_3/NiFe_2O_4$ PNTs and $SrTiO_3/NiFe_2O_4$ PITs, respectively. When the two composite photocatalysts are irradiated by the incident photons (hv) with enough energies, the electrons (e^-) located on the valance bands (VB) of $SrTiO_3$ component or $NiFe_2O_4$ component absorb the photons and transits the bad gaps (3.2 and 1.7 eV calculated for $SrTiO_3$ and $NiFe_2O_4$, respectively) and then arrive at the conduction band (CB). And an equal number of holes (h^+) are left on the CB. Subsequently, the photo-excited carriers immediately migrate to the photocatalysts surface to involve in the catalytic reaction. However, during the photo-excited h^+ and e^- generation, their recombination also occurs simultaneously. Based on the previous reports, the CB

minimum and VB maximum of $SrTiO_3$ are both lower than that of $NiFe_2O_4$.[36,33] In the case of the $SrTiO_3/NiFe_2O_4$ PNTs (Fig. 6(h)), therefore, a build-in internal electric field is formed in the heterojunctions between $SrTiO_3$ and $NiFe_2O_4$ nanoparticles. Under the assistance of the internal electric field, the h^+ on the VB of $SrTiO_3$ rises to that of $NiFe_2O_4$ and the e^- on the CB of $NiFe_2O_4$ drops to that of $SrTiO_3$. And the resultant h^+ on the VB of $NiFe_2O_4$ can't recombine with the e^- on the CB of $SrTiO_3$. As thus, such behaviour promotes the separation of photo-excited h^+ and e^- and then increases their survival probability. In the $SrTiO_3/NiFe_2O_4$ PITs case (Fig. 6(i)), nevertheless, there is no such an internal electric field between $SrTiO_3$ and $NiFe_2O_4$ nanoparticles. As a consequence, the $SrTiO_3/NiFe_2O_4$ PNTs perform a higher photocatalytic activity than that of the PITs.
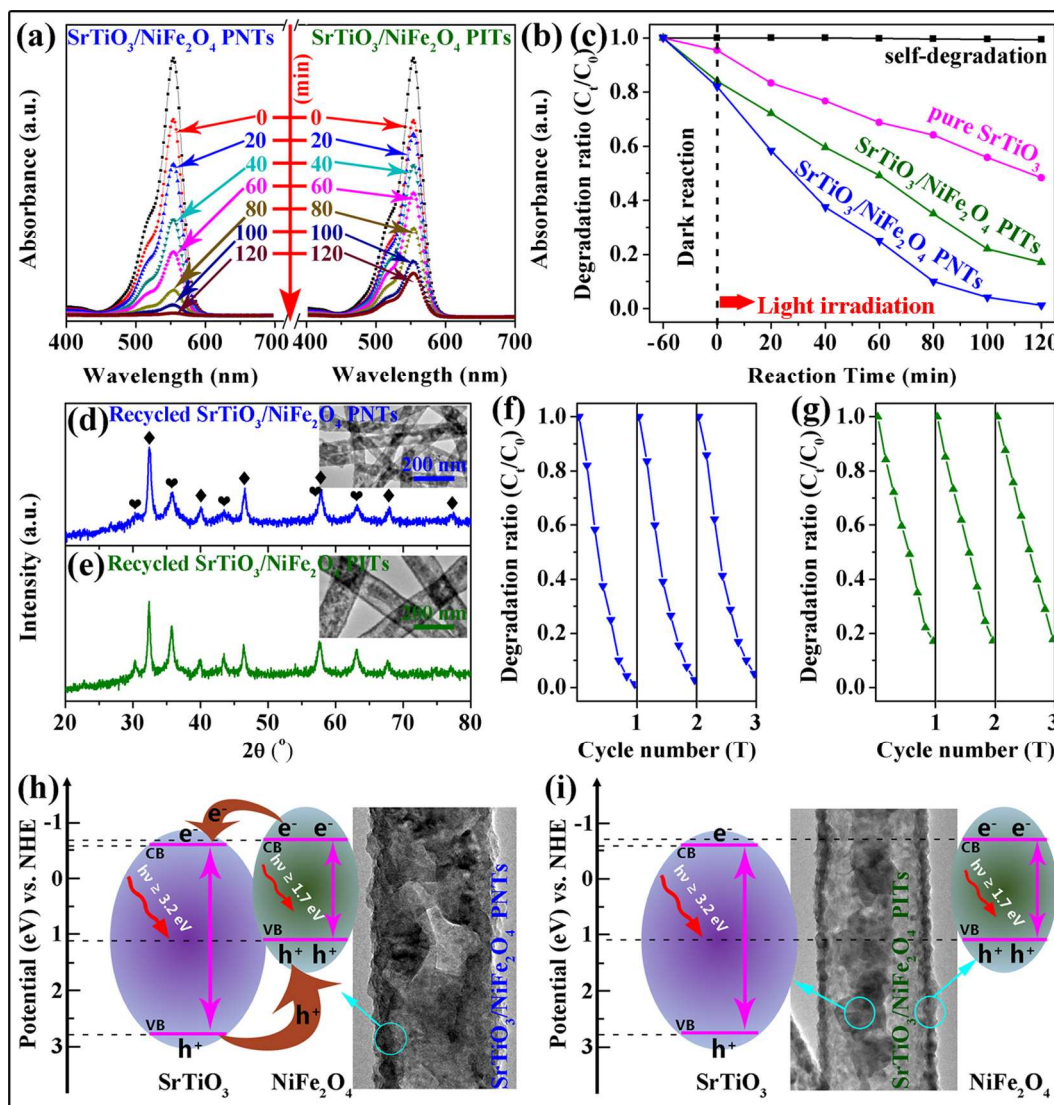

Fig. 6 (a) and (b) Time-dependant absorption spectra of RhB solution over the $SrTiO_3/NiFe_2O_4$ PNTs and $SrTiO_3/NiFe_2O_4$ PITs, respectively. (c) Photocatalytic efficiency of RhB solutions with or without photocatalysts as a function of light irradiation time. (d) and (e) XRD patterns and SEM images of the recycled $SrTiO_3/NiFe_2O_4$ PNTs and $SrTiO_3/NiFe_2O_4$ PITs after the first reaction. (f) and (g) Cycling tests of the same batch $SrTiO_3/NiFe_2O_4$ PNTs and the $SrTiO_3/NiFe_2O_4$ PITs for the degradation of RhB. (h) and (i) Schematic illustrations of the energy band structures and the photon-excited h^+ and e^- separation in the $SrTiO_3/NiFe_2O_4$ PNTs and $SrTiO_3/NiFe_2O_4$ PITs.

Although such interesting features of the $SrTiO_3/NiFe_2O_4$ PNTs and $SrTiO_3/NiFe_2O_4$ PITs are separately similar to the TiO_2/CuO PNTs and $Ni_{0.5}Zn_{0.5}Fe_2O_4/Ni_{0.5}Zn_{0.5}Fe_2O_4$ wire-in-tubes,[41,42] their

possible formation mechanisms should still be clarified. Based on the schematic diagram shown in Fig. 7(a), the formation mechanism of the $SrTiO_3/NiFe_2O_4$ PNTs is proposed as below. As previous

studies indicated, most of the electrospun nanostructures are originated from the so-called "Taylor-cone".[12] In Fig. 7(a1), a Taylor-cone is formed in the single-spinneret tip under the joint result of the electrostatic field force and surface tension. When the electrostatic field force overcomes the surface tension, a charged jet-flow (Fig. 7(a2)) with uniform chemical contents (PVP, $Fe(NO_3)_3$, $Ni(NO_3)_2$, $Sr(NO_3)_2$, $Ti(C_4H_9O)_4$) rapidly spews out from the Taylor-cone and is stretched to the nanofiber further. In a stretched forward nanofiber, solvents volatilization is an important factor. Generally, the surface solvent volatilization is faster than the internal solvent volatilization and the solvent content will gradually decrease from centre to surface. Then a solvent content-gradient is formed and it can cause the sportive nanofiber system into an extremely unstable state. In this situation, furthermore, the solvent volatilization could offer a driving force for the other salt ions. Accompanied by the solvent motion, therefore, the salts of $Sr(NO_3)_2$, $Ni(NO_3)_2$, $Fe(NO_3)_3$ and $Ti(C_4H_9O)_4$ can be together migrated to the outer layer of nanofiber, as shown in the Fig. 7(a3). When the solvents volatilize completely, the PVP-core/$[Ti(C_4H_9O)_4+$nitrates$+PVP]$-shell precursor nanofibers (Fig. 7(a4)) deposit on the collector. After annealing the as-spun core-shell nanofibers at high temperature of 650 ^{o}C to remove the PVP-core, finally, the $SrTiO_3/NiFe_2O_4$ PNTs (Fig. 7(a5)) are obtained. The above potential formation mechanism is assumed according to the "self-template effect".[40] Nevertheless, the formation mechanism of the $SrTiO_3/NiFe_2O_4$ PITs is somewhat different and the schematic diagram is presented in Fig. 7(b). Firstly, it should be noted that the main function of acetic acid in the spinning solution is to inhibit the hydrolysis of $Ti(C_4H_9O)_4$. For the $SrTiO_3/NiFe_2O_4$ PITs, the chemical reagents of the Taylor-cone (Fig. 7(b1)) come from two sources. One source contains $Fe(NO_3)_3$, $Ni(NO_3)_2$, water, DMF and ethanol, but another contains $Sr(NO_3)_2$, ethanol, $Ti(C_4H_9O)_4$ and acetic acid. Due to the uneven distribution and rapid volatilization of acetic acid, the $Ti(C_4H_9O)_4$ can be hydrolyzed instantaneously into the $Ti(OH)_4$ once the flow-jet (Fig. 7(b2)) ejected from its Taylor-cone. Secondly, when $Sr(NO_3)_2$, $Ni(NO_3)_2$, $Fe(NO_3)_3$ are outward migrated to the nanofiber surface, while the $Ti(OH)_4$ would inward diffuse to the centre continually (Fig. 7(b3)). In fact, the diffusion principle of Kirkendall-effect indicates that the hydroxides $(Ti(OH)_4)$ can refill the internal vacancies left by nitrates in a non-equilibrum multi-component mixture.[43] After the solvent volatilized completely, as well, the $[PVP+Ti(OH)_4]$-core/$[$nitrates$+PVP]$-shell nanofibers (Fig. 7(b4)) are deposit on the collector. Thirdly, during the as-spun composite nanofibers are annealed at 650 ^{o}C, the PVP is decomposed, $Fe(NO_3)_3$ and $Ni(NO_3)_2$ are compounded to $NiFe_2O_4$ nanoparticles constructing the nanotube. Meanwhile, $Sr(NO_3)_2$ diffuses inward to the internal $Ti(OH)_4$ and generates $SrTiO_3$ nanoparticles based on the phase separation. Finally, the $SrTiO_3/NiFe_2O_4$ PITs are obtained, as shown in Fig. 7(b5).
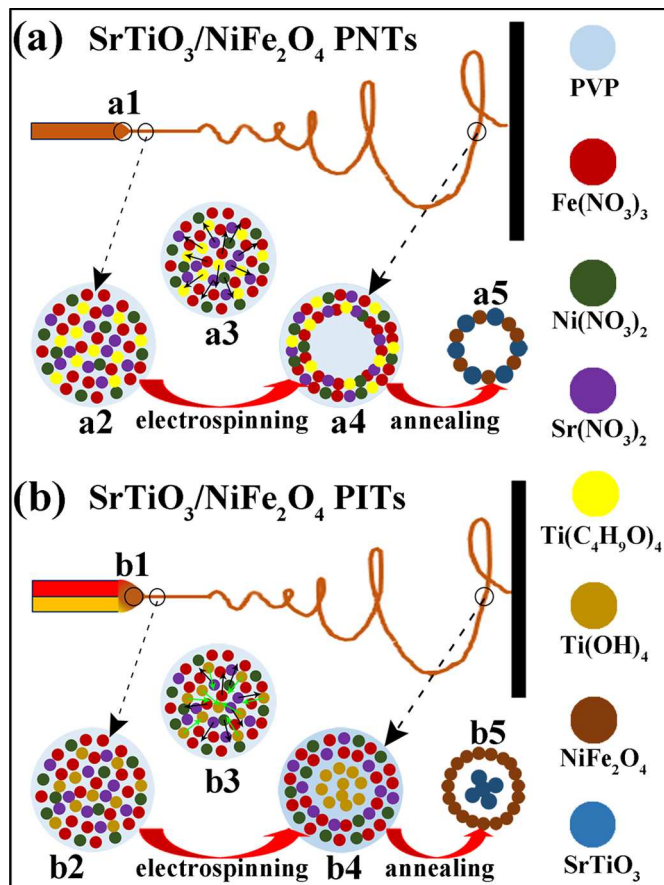

Fig. 7 Formation mechanism diagrams for (a) $SrTiO_3/NiFe_2O_4$ PNTs and (b) $SrTiO_3/NiFe_2O_4$ PITs.

Conclusion

In summary, $SrTiO_3/NiFe_2O_4$ PNTs and $SrTiO_3/NiFe_2O_4$ PITs have been successfully prepared for the first time by using a single-spinneret electrospinning and a modified side-by-side-spinneret electrospinning, respectively. It demonstrates that the $SrTiO_3/NiFe_2O_4$ PNTs is composed of numerous heterojunctions of perovskite $SrTiO_3$ and spinel $NiFe_2O_4$ nanoparticles, but the $SrTiO_3/NiFe_2O_4$ PITs is self-organized by embedding $SrTiO_3$ nanoparticles into $NiFe_2O_4$ nanotube. Both of the two $SrTiO_3/NiFe_2O_4$ composites not only exhibit a well-dispersive hollow structure and a powerful response to the UV and visible-light, but also show a good room temperature ferromagnetism and an amazing magnetic separation efficiency. Furthermore, the two magnetic composites both perform a considerable photocatalytic activity in the degradation of RhB. Especially, we believe that this work could offer a simple method to prepare a self-assembled composite nanostructure of different nanomaterials.

Notes and references

[a] Key Laboratory for Magnetism and Magnetic Materials of Ministry of Education, Lanzhou University, Lanzhou, 730000, People's Republic of China

[b] Key Laboratory of Special Function Materials and Structure Design of the Ministry of Education, Lanzhou University, Lanzhou 730000, People's Republic of China

Nanoscale Accepted Manuscript

*Corresponding author: E-mail: liuqf@lzu.edu.cn

1. G. R. Yang, W. Yan, Q. Zhang, S. H. Shen and S. J. Ding, *Nanoscale*, 2013, **5**, 12432-12439.

2. T. Tran, K. McCormac, J. L. Li, Z. H. Bi and J. Wu, *Electrochimica Acta*, 2014, **117**, 68-75.

3. B. T. Song, C. T. Wu and J. Chang, *Acta biomaterialia*, 2012, **8**, 1901-1907.

4. L. Liu, Y. Zhang, G. G. Wang, S. C. Li, L. Y. Wang, Y. Han, X. X. Jiang and A. G. Wei, *Sensors and Actuators B: Chemical*, 2011, **160**, 448-454.

5. X. Q. Shen, F. Z. Song, X. C. Yang, Z. Wang, M. X. Jing and Y. D. Wang, *Journal of Alloys and Compounds*, 2015, **621**, 146-153.

6. P. Poudel and Q. Q. Qiao, *Nanoscale*, 2012, **4**, 2826-2838.

7. H. Huang, X. Feng and J. J. Zhu, *Nanotechnology*, 2008, **19**, 145607.

8. S. S. Jyothirmayee Aravind, V. Eswaraiah and S. Ramaprabhu, *Journal of Materials Chemistry*, 2011, **21**, 15179.

9. X. F. Liu, X. R. Cui, X. B. Chen, N. Yang and R. H. Yu, *Materials Research Bulletin*, 2014, **50**, 113-117.

10. Z. X. Dong, S. J. Kennedy and Y. Q. Wu, *Journal of Power Sources*, 2011, **196**, 4886-4904.

11. R. Rojas and N. J. Pinto, *IEEE Sensors Journal*, 2008, **8**, 951-953.

12. X. L. Hu, S. Liu, G. Y. Zhou, Y. B. Huang, Z. G. Xie and X. B. Jing, *Journal of controlled release*, 2014, **185**, 12-21.

13. X. F. Wang, B. Ding and B. Y. Li, *Materials today*, 2013, **16**, 229-241.

14. A. V. Bazilevsky, A. L. Yarin and C. M. Megaridis, *Langmuir*, 2007, **23**, 2311-2314.

15. K. M. Forward, A. Flores and G. C. Rutledge, *Chemical Engineering Science*, 2013, **104**, 250-259.

16. T. Fiorido, J. Galineau, V. Salles, L. Seveyrat, F. Belhora, P.-J. Cottinet, L. Hu, Y. Liu, B. Guiffard, A. B.-V. D. Moortele, T. Epicier, D. Guyomar and A. Brioude, *Sensors and Actuators A: Physical*, 2014, **211**, 105-114.

17. T. T. Jiang, Z. J. Wang, Z. Y. Li, W. Wang, X. R. Xu, X. Liu, J. F. Wang and C. Wang, *Journal of Materials Chemistry C*, 2013, **1**, 3017-3025.

18. Z. Y. Liu, D. D. Sun, P. Guo and J. O. Leckie, *Nano Letters*, 2007, **7**, 1081-1085.

19. F. Xu, L. M. Li and X. J. Cui, *Journal of Nanomaterials*, 2012, **2012**, 1-5.

20. R. Andreozzi, V. Caprio, A. Insola and R. Marotta, *Catalysis Today*, 1999, **5**, 51-59.

21. S. Senapati, S. K. Srivastava and S. B. Singh, *Nanoscale*, 2012, **4**, 6604-6612.

22. J. Q. Zheng, Y. J. Zhu, J. S. Xu, B. Q. Lu, C. Qi, F. Chen and J. Wu, *Materials Letters*, 2013, **100**, 62-65.

23. H. Yu, S. C. Yan, Z. S. Li, T. Yu and Z. G. Zou, *International Journal of Hydrogen Energy*, 2012, **37**, 12120-12127.

24. P. P. Jing, J. N. Li, L. N. Pan, J. B. Wang, X. J. Sun and Q. F. Liu, *Journal of hazardous materials*, 2015, **284**, 163-170.

25. X. H. Li, Y. C. Zhang, H. Y. Li, H. B. Chen, Y. M. Ding and W. M. Yang, *Desalination*, 2014, **344**, 266-273.

26. H. M. A. Asghar, S. N. Hussain, E. P. L. Roberts, A. K. Campen and N. W. Brown, *Journal of Industrial and Engineering Chemistry*, 2013, **19**, 1689-1696.

27. X. Cao, Y. Chen, S. H. Jiao, Z. X. Fang, M. Xu, X. Liu, L. Li, G. S. Pang and S. H. Feng, *Nanoscale*, 2014, **6**, 12366-12370.

28. F. Z. Mou, L. L. Xu, H. R. Ma, J. G. Guan, D. R. Chen and S. H. Wang, *Nanoscale*, 2012, **4**, 4650-4657.

29. C. Y. Wang, L. Y. Zhu, C. Chang, Y. Fu and X. L. Chu, *Catalysis Communications*, 2013, **37**, 92-95.

30. A. W. Sun, H. Chen, C. Song, F. Jiang, X. Wang and Y. S. Fu, *RSC Advances*, 2013, **3**, 4332.

31. P. Sivakumar, R. Ramesh, A. Ramanand, S. Ponnusamy and C. Muthamizhchelvan, *Journal of Alloys and Compounds*, 2013, **563**, 6-11.

32. M. W. Kadi and R. M. Mohamed, *Ceramics International*, 2014, **40**, 227-232.

33. A. Ren, C. B. Liu, Y. Z. Hong, W. D. Shi, S. Lin and P. Li, *Chemical Engineering Journal*, 2014, **258**, 301-308.

34. H. S. Kim, D. Kim, B. S. Kwak, G. B. Han, M.-H Um and M. Kang, *Chemical Engineering Journal*, 2014, 243, 272-279.

35. U. Holzwarth and N. Gibson, *Nature nanotechnology*, 2011, **6**, 534.

36. P. Reunchan, S. X. Ouyang, N. Umezawa, H. Xu, Y. J. Zhang and J. H. Ye, *Journal of Materials Chemistry A*, 2013, **1**, 4221.

37. A. Tumuluri, K. L. Naidu and K. C. J. Raju, *International Journal of ChemTech Reaserch*, 2014, **6**, 3353-3356.

38. H. S. Kim, D. Kim, B. S. Kwak, G. B. Han, M.-H. Um and M. Kang, *Chemical Engineering Journal*, 2014, **243**, 272-279.

39. Y. Li, X. F. Dong and J. P. Li, *Particuology*, 2011, **9**, 475-479.

40. H. Wang, X. Guo, S. Fu, T. Yang, Y. Wen and H. Yang, *Food Chemistry,* 2015, 188137-142.

41. S. S. Lee, H. W. Bai, Z. Y. Liu and D. D. Sun, *Applied Catalysis B: Environmental*, 2013, **140-141**, 68-81.

42. J. C. Fu, J. L. Zhang, Y. Peng, C. H. Zhao, Y. M. He, Z. Zhang, X. Pan, N. J. Mellors and E. Xie, *Nanoscale*, 2013, **5**, 12551-12557.

43. H. J. Fan, M. Knez, R. Scholz, K. Nielsch, E. Pippel, D. Hesse, M. Zacharias and U. Gosele, *Nat Mater*, 2006, **5**, 627-631.

Nanoscale Accepted Manuscript